Available online at www.sciencedirect.com
ScienceDirect
Remote Sensing of Environment 107 (2007) 299–311
Remote Sensing of Environment
www.elsevier.com/locate/rse

Support vector machines for recognition of semi-arid vegetation types using MISR multi-angle imagery

Lihong Su [a,*], Mark J. Chopping [a], Albert Rango [b], John V. Martonchik [c], Debra P.C. Peters [b]

[a] Department of Earth and Environmental Studies, Montclair State University, Montclair, New Jersey 07043, USA
[b] USDA, ARS Jornada Experimental Range, Las Cruces, New Mexico 88003, USA
[c] NASA Jet Propulsion Laboratory, Pasadena, California 91109, USA

Received 22 December 2005; received in revised form 28 April 2006; accepted 7 May 2006

Abstract

Accurately mapping community types is one of the main challenges for monitoring arid and semi-arid grasslands with remote sensing. The multi-angle approach has been proven useful for mapping vegetation types in desert grassland. The Multi-angle Imaging Spectro-Radiometer (MISR) provides 4 spectral bands and 9 angular reflectance. In this study, 44 classification experiments have been implemented to find the optimal combination of MISR multi-angular data to mine the information carried by MISR data as effectively as possible. These experiments show the following findings: 1) The combination of MISR's 4 spectral bands at nadir and red and near infrared bands in the C, B, and A cameras observing off-nadir can obtain the best vegetation type differentiation at the community level in New Mexico desert grasslands. 2) The k parameter at red band of Modified–Rahman–Pinty–Verstraete (MRPV) model and the structural scattering index (SSI) can bring useful additional information to land cover classification. The information carried by these two parameters, however, is less than that carried by surface anisotropy patterns described by the MRPV model and a linear semi-empirical kernel-driven bidirectional reflectance distribution function model, the RossThin–LiSparseMODIS (RTnLS) model. These experiments prove that: 1) multi-angular reflectance raise overall classification accuracy from 45.8% for nadir-only reflectance to 60.9%. 2) With surface anisotropy patterns derived from MRPV and RTnLS, an overall accuracy of 68.1% can be obtained when maximum likelihood algorithms are used. 3) Support Vector Machine (SVM) algorithms can raise the classification accuracy to 76.7%. This research shows that multi-angular reflectance, surface anisotropy patterns and SVM algorithms can improve desert vegetation type differentiation importantly.

Keywords: MISR; Support vector machine; Semi-arid vegetation; Classification; Multi-angle observations

1. Introduction

New sensor and new classification methods in remote sensing are providing capabilities for mapping and monitoring the desert environment as never before. A plant community type may be defined as an aggregation of plant types, which demonstrate mutual interrelationships between species and between species and the environment. Community type differentiation is a classification problem in which the classes are the recognized plant community types and also is an approach to monitoring semi-arid grasslands. It implies a larger number of classes, which differ more subtly than the broader categories assigned to regional or global classification schemes (Chopping et al., 2002).

This study emphasizes a distinctive capability provided by surface reflectance anisotropy patterns for community and cover type monitoring. Our approach is based on an analysis of 1) data acquired by Multi-angle Imaging Spectro-Radiometer (MISR) on NASA's Earth Observing System (EOS) Terra satellite, 2) surface anisotropy patterns estimated via inversion of the Modified Rahman–Pinty–Verstraete (MRPV) model (Engelsen et al., 1996) and a linear semi-empirical kernel-driven model (Wanner et al., 1995), the RossThin–LiSparseMODIS (RTnLS) model on MISR red and near infrared wavelength data. All surfaces, including natural and man-made, show some degree of spectral reflectance anisotropy when illuminated by sunlight. The surface anisotropy patterns depend on the three-

* Corresponding author.
E-mail address: sul@mail.montclair.edu (L. Su).

0034-4257/$ - see front matter © 2006 Elsevier Inc. All rights reserved.
doi:10.1016/j.rse.2006.05.023

dimensional structure and optical properties of the surface. This implies that the surface anisotropy patterns can be used to characterize the surface target; so it should be reasonable to introduce the surface anisotropy patterns into the classification experiment. The anisotropic behavior of surface reflectance is described by the Bidirectional Reflectance Distribution Function (BRDF); surface anisotropy patterns can be encapsulated in the parameters of a BRDF model.

This study also investigates some indices derived from BRDF computation, such as parameter k of the MRPV model (Pinty et al., 2002), the structural scattering index (SSI) (Gao et al., 2003). These indices have been proposed as means to access surface heterogeneity at the subpixel level. The main goal of this study is to: 1) analyze the applicability of the newly acquired MISR data; 2) evaluate the usability of surface anisotropy patterns derived from these two main operational BRDF models in classification; and 3) review the accuracy improvement of the support vector machine (SVM) algorithm. The following is a brief introduction to the MRPV model and the linear semi-empirical kernel-driven model.

1.1. MRPV model and its k parameter at red band

The Modified Rahman–Pinty–Verstraete (MRPV) model (Diner et al., 1999; Engelsen et al., 1996) is a modified version of the Rahman–Pinty–Verstraete (RPV) model (Rahman et al., 1993a,b). This model estimates the bi-directional reflectance factor (BRF) of an arbitrary surface as a function of the geometry of illumination and viewing, as well as uses the following three parameters to describe the anisotropy of the surface:

1) $\rho 0$, giving the overall reflectance level;
2) k, a representative of the bowl or bell shape of the surface anisotropy;
3) b, describing the predominance of forward or backward scattering.

Based on the extensive 3-dimensional radiation transfer simulations, the parameter k at red wavelength of the MRPV model was proven to be capable to reveal surface cover heterogeneity at the subpixel level (Pinty et al., 2002). The underlying physics is that for typical vegetation systems, measurements in the red spectral region permit maximizing the contrast between the scattering/absorption properties over the vegetation stands versus the underlying soil. The value of the parameter k at red wavelength can be explained as below.

- $k<1.0$ means a bowl-shape anisotropy pattern where BRF values close to nadir are lower than larger exiting angles.
- $k=1.0$ indicates a Lambertian surface, an idealized case rarely found in practice.
- $k>1.0$ means a bell-shape anisotropy pattern where BRF values measured at large exiting angles are lower than those measured at angles close to nadir.

The terrestrial surface usually exhibits a bowl-shape anisotropy pattern. This situation is generally observed for thick homogeneous plant canopies, bare soil, and other planetary surfaces as well. Some terrestrial surfaces will exhibit a bell-shape anisotropy pattern. This situation is generally observed for sparse coniferous forest over a bright snow background, or sparse bushes over a bright sandy desert at red wavelengths. In such cases, the high background reflectance dominates at small viewing zenith angles, while the absorbing properties of the dark objects control the reflectance of the entire scene at large angles. The parameter k was proposed as a new axis of information in addition to the classical spectrally derived information (Pinty et al., 2002).

1.2. The semi-empirical kernel-based BRDF model and structural scattering index

Physical BRDF models relate the reflectance anisotropy of a remotely-sensed pixel to the biogeophysical, structural, and component spectral information in the pixel. A kernel-driven semi-empirical BRDF model was first derived from a physically-based BRDF model by Roujean et al. (1992) and developed further by Wanner et al. (1995). These models use fewer model parameters than true physical models and have a simple linear form (Eq. (1)):

$$\mathrm{BRDF} = f_{\mathrm{iso}} + f_{\mathrm{vol}} * k_{\mathrm{vol}}(\theta_i, \theta_v, \phi) + f_{\mathrm{geo}} * k_{\mathrm{geo}}(\theta_i, \theta_v, \phi) \quad (1)$$

where, k_{vol}, called volumetric kernel, is a function of view zenith θ_{v} illumination zenith θ_{i} and relative azimuth ϕ. The k_{vol} describes the volume scattering from the pixel. k_{geo}, called geometric kernel, also is a function of the θ_{v}, θ_{i} and ϕ. The k_{geo} describes the surface scattering from the pixel. f_{vol} and f_{geo} are the weights for these two kernels, respectively. f_{iso} represents isotropic reflectance. As the study area is a semi-arid region in this research, we selected RossThin kernel as k_{vol}, and LiSparseMODIS kernel as k_{geo}, partly because this combination produces fewer negative kernel weights (Chopping, 2001). The semi-empirical kernel-driven BRDF model with RossThin and LiSparseMODIS kernels is abbreviated here as RTnLS. We used a modified version of the Algorithm for MODIS Bidirectional Reflectance Anisotropies of the Land Surface (AMBRALS) (Schaaf et al., 2002; Strahler & Muller, 1999), version 2.4 to adjust the RTnLS model against MISR multi-angle data sets.

When a physical BRDF model is simplified as a semi-empirical kernel-based BRDF model, the relationship between the BRDF and vegetation structure is no longer clear (Su et al., 2002). To reveal this relationship, a structural scattering index (SSI) was proposed by Gao et al. (2003). The structural scattering index (SSI) is (Eq. (2)):

$$\mathrm{SSI} = \ln(f_{\mathrm{vol}}^{\mathrm{nir}} / f_{\mathrm{geo}}^{\mathrm{red}}) \quad (2)$$

where $f_{\mathrm{vol}}^{\mathrm{nir}}$ is the volumetric weight for the near infrared band and $f_{\mathrm{geo}}^{\mathrm{red}}$ is the geometric weight for the red spectral band retrieved by adjusting the model against a set of bidirectional reflectance. The reflectance anisotropy in the near infrared band, described by the volumetric scattering kernel, will be

decreased by high multiple scattering within the canopy due to the high leaf transmittance as well as reflectance in the near infrared band for vegetation leaves. Conversely, the reflectance anisotropy in the red band, described by the geometric scattering kernel, will be increased by small leaf transmittance and reflectance at the red band due to chlorophyll absorbance. Therefore the SSI should be sensitive to vegetation structure. Preliminary investigations show that the SSI can be used to distinguish different land cover types or to detect structural changes; it has thus has been proposed as a source of extra structural information for classification (Gao et al., 2003).

2. Study area

Our study area lies within the Chihuahuan semi-desert province, which in the United States stretches across south-eastern Arizona, southern New Mexico, and western Texas. The specific study sites are the Jornada Experimental Range in southern New Mexico near Las Cruces (a USDA, Agricultural Research Service (ARS) and National Science Foundation (NSF) Long Term Ecological Research (LTER) site and a NASA EOS Land Validation Core site, centered at 32.5° N, 106.8° W; Morisette et al., 1999); and the Sevilleta National Wildlife Refuge in central New Mexico near Albuquerque (an LTER, US Fish and Wildlife Service, and a NASA EOS Land Validation Core Site, centered at 32.5° N, 106.8° W; Ritchie et al., 2000). The Jornada Experimental Range is about 78,266 ha, locating between the Rio Grande floodplain on the west and the crest of the San Andres Mountains on the east. Its mean elevation is about 1350 m. The Sevilleta National Wildlife Refuge is approximately 100,000 ha in size, encompassing two mountain ranges and the Rio Grande valley in between. It lies at the junction of several major biomes of the American Southwest with an elevation range from 1350 to 2797 m.

The climate at the two intensive study sites is characterized by high amounts of solar radiation, wide diurnal ranges of temperature, low relative humidity, extremely variable precipitation (spatially and temporally), and high potential rates of evaporation. The dry early-summer months of May and June are typically the hottest part of the year in the Chihuahuan Desert. Average annual precipitation is about 230 mm. Typically more than 50% of rainfall occurs from July to October as convective events. In this research, we selected MISR data from May 24 to June 3, 2002, as this time is the end of dry season and all shrubs are leafed out but grasses and some other small plants are mostly dormant.

Shrubs are now the dominant plants in the Chihuahuan desert. They frequently grow in open stands. In many places, they are associated with short grasses, such as black grama (*Bouteloua eriopoda*). In this research, we used two existing vegetation maps as reference data. The first one is the Sevilleta National Wildlife Refuge vegetation map. This map was created based on an unsupervised classification of 12 multi-temporal Landsat Thematic Mapper satellite images that variously cover the April-to-October growing seasons from 1987 to 1993. The Sevilleta vegetation map has 13 map classes based on similar vegetation composition and spatial relationships. This vegetation map is provided in raster data format, having nominal 0.5 ha resolution (Muldavin et al., 1998). The Jornada Experimental Range vegetation map (vector format) was created from 1998 aerial photography and field data (Nolen et al., 1999). The map has 9 classes each of which has a unique species composition and dominant species; these classes therefore describe the major plant communities. This vegetation map is provided in vector data format, and its smallest polygon has an area of 2992.7 m^2. Intensive fieldwork has been carried out at both sites (Muldavin et al., 1998; Rango et al., 1998).

3. Methods

This section is divided into three parts: Section 3.1 introduces the data which were used and the classifications carried out; Section 3.2 presents briefly how MISR data were processed; and Section 3.3 explains how SVM was used to obtain the classifications.

3.1. Data and experiment description

MISR multi-angular reflectance is the main data used. The MISR instrument provides new and unique opportunities to record the anisotropy of land surfaces by quasi-simultaneous observations in 4 spectral bands (blue, green, red and near infrared) at nadir and 8 off-nadir observations (26.1, 45.6, 60.0 and 70.5° from the vertical both forward and afterward of nadir in the satellite along-track direction). In order to mine the information carried by multi-angular data as effectively as possible, we used maximum likelihood classification (MLC) and support vector machine (SVM) methods to perform 44 experiments on 30 data sets. These 44 experiments fall into 6 groups, which are listed in Tables 2–7. These 30 data sets consist of various combinations of MISR nadir and off-nadir reflectance, the k parameter at red band of the MRPV model, SSI, and surface anisotropy patterns described by both the MRPV model and the RTnLS model ($\rho 0$, k, b and iso, vol, geo, respectively).

We used MLC methods to classify vegetation types at the community level with various combinations of MISR 4 spectral bands at nadir viewing and red and near infrared bands viewing off-nadir. In order to evaluate the usability of the k parameter, SSI, and surface anisotropy patterns derived from the MRPV and the RTnLS models, we also used MLC to classify vegetation types with various combinations of these parameters and MISR reflectance. In order to review the accuracy improvement of the SVM algorithms, we used SVM algorithms to carry out classifications with same data sets as with the MLC methods. The overall accuracy and Kappa index were calculated for every case. For maximum likelihood classifications, the separability is also given based on the transformed divergence (TD). This transformed divergence will always be incremental when the bands are added, so the transformed divergence does not keep a constant relationship with classification accuracy (Jensen, 1996).

This study used 3 MISR data products: 1) MISR level 1B2 MI1B2T terrain-projected product, 2) MISR Level 1B2

MI1B2GEOP Geometric parameters product, and 3) MISR Level 2 MIL2ASAE aerosol product. The MI1B2T product is the terrain-projected top-of-atmosphere (TOA) radiance global mode parameter. This TOA radiance has had a geometric correction applied, which removes the errors of spacecraft position and pointing knowledge and errors due to topography. The parameter is then ortho-rectified on a reference ellipsoid at the surface. This global mode parameter is averaged to 1.1 km resolution in the off-nadir, non-red band channels. The MI1B2GEOP product provides solar azimuth, solar zenith, and MISR 9 cameras azimuth and zenith at 17.6 km resolution. The MIL2ASAE product provides regional mean spectral optical depth at MISR 4 bands with 17.6 km resolution. The detailed information about these three products can be found in MISR Data Products Specifications (Lewicki et al., 2003). In order to share our experiences with MISR multi-angular data processing, we give a brief description of our processing approach in Section 3.2 which is expanded in Appendix A.

This study used both MLC and SVM algorithms for classification. The MLC assumes that each spectral class can be described by a probability distribution in multi-spectral space. Such a distribution describes the chance of finding a pixel belonging to that class at any given location in multi-spectral space. SVM algorithms are inspired by statistical learning theory (Vapnik, 1995) and do not use the probability distribution of a spectral class: it is a non-parametric method. Unlike maximum likelihood classification, SVM is not yet used extensively in remote sensing classification though its use is increasing. Published studies report that SVM has been applied successfully to classification problems (Huang et al., 2002; Keuchel et al., 2003; Pal & Mather, 2005; Zhu & Blumberg, 2002). The implementation of the SVM algorithm used in this research is described in Section 3.3.

3.2. MISR data preprocessing

The upper-left corner of our working region is at 35° N, 108° W, and the lower-right corner is at 31.2° N, 105.5° W. From May 22 to June 3, there were 5 orbits overlapping the working region. They are: O012937 (2002-05-24); O012981 (2005-05-27); O013010, (2002-05-29); O013039 (2002-05-31); and O013068 (2002-06-02). Among these 5 orbits, only O013039 covers both study sites: the Jornada and the Sevilleta. The MISR data were resampled to a 250 m spatial resolution in order to enable data fusion research. Below we first recall the fundamental parameters of the MISR instrument and its data product format and coordinate transformation; we then describe briefly two key steps of the MISR data processing: resample and atmospheric correction. The specific procedures employed in processing the three MISR data products are described in Appendix A.

MISR employs nine discrete cameras to acquire images along the Terra ground track. These cameras point at fixed angles, one viewing in the nadir direction (vertically downward, designed An camera) and four viewing in the forward (designed Af, Bf, Cf, and Df camera) and afterward (designed Aa, Ba, Ca, and Da camera) directions at 26.1, 45.6, 60.0, and 70.5° respectively. The MISR cameras image at four spectral bands with center wavelengths at 446, 558, 672, and 867 nm. In Global Science mode, the MISR nadir camera produces 275 m resolution images at all four bands. The 8 off-nadir cameras produce 275 m resolution data in the red band (only) and 1.1 km resolution images in the blue, green and near infrared bands. MISR uses 233 paths in Terra's sun-synchronous orbits to cover the Earth and acquires data continuously down the entire daylit side of each orbit. The resulting image swath product is 360 km wide by about 20,000 km long.

MISR has a specific Space Oblique Mercator (SOM) projection applicable to each path. In SOM coordinates, the X axis points more or less in the direction of satellite ground track motion, with the Y axis perpendicular to X axis. The pixels in a MISR swath are arranged in a regular two-dimensional array in the SOM space. The indices to the array are called absolute line and sample, which references the specific SOM projection of every path. MISR uses 180 pre-defined blocks in fixed geographic locations to cover the full extent of the swaths. A block may be placed directly beneath the one above it, or it may be shifted by an integral multiple of 17.6 km in the lateral (± SOM Y axis) direction. These shifts are pre-defined so that the blocks comfortably span the Terra ground track to encompass a MISR data swath. Each block may be treated by the user as an independent two-dimensional array. The block-relative line and sample restart at 0, 0 at the top left corner of each block. Therefore, the geographic coordinates of a given pixel in a MISR data swath can be determined through three phases like this: (block, block-relative line, block-relative sample)<–phase 1–>(absolute line, absolute sample)<–phase 2–>SOM (X, Y)<–phase 3–>(latitude, longitude). The phase 1 processing needs the pre-defined block shift array of the path (it is worth noting that the block array employs a zero-based index and block offset array uses a 1-based index). The phase 2 processing requires the SOM projection parameters of the path. In phase 3, the General Cartographic Transformation Package (GCTP) coordinate conversion software of the U.S. Geological Survey was used to convert between SOM coordinates and Latitude/Longitude.

Atmospheric corrections transferred the TOA radiance provided by the MI1B2T product to surface reflectance. The computation used the viewing and solar angles provided by the MI1B2GEOP product and the optical depth of aerosol provided by the MIL2ASAE product. Both of MI1B2GEOP and MIL2ASAE data have 17.6 km resolution while MI1B2T data have 275 m or 1.1 km resolution. Moreover, one 17.6 km pixel exactly covers 16*16 (256) 1.1 km pixels or 64*64 (4096) 275 m pixels in the MISR products. This means that 256 or 4096 TOA radiances have same aerosol parameters, solar angles, and observing angles. So we performed atmospheric correction based on 17.6 km pixels. For each 17.6 km pixel, the atmospheric correction includes: a) sort the 256 or 4096 TOA radiances covered by the pixel; b) select 16 TOA radiances uniformly; c) run the Simple Method for Atmospheric Correction (SMAC; Rahman & Dedieu, 1994) for the 16 radiances to calculate their ground reflectance; d) regress these TOA radiances and their ground reflectance and e) apply the

regression parameters to all other TOA radiances to obtain their ground reflectance. Following TOA radiances, the surface reflectance is indexed by MISR (block, block-relative line, block-relative sample) coordinates. This regression approach was compared with directly running SMAC on 275 m or 1.1 km TOA radiances pixel by pixel. Their correlation coefficient always is greater than 0.99975 and standard error is less than 0.000003. The absolute error always is less than 0.001 for any pixel. This atmospheric correction approach works well within the constraints of the available atmospheric data.

We also tested the SMAC version 4 code against 6S version 4.2 (Vermote et al., 1997) for a selection of six contrasting surfaces ranging from very dark to very bright: Elephant Butte lake (dark target); two lava flows (dark target); Jornada (desert target); Sevilleta (desert target); and White Sands alkali flats (bright target). The atmosphere potentially has a large impact on the accuracy of surface bi-directional spectral reflectance at large sensor zenith angles such as those of the MISR D cameras. We therefore assessed the quality of the SMAC and 6S atmospheric corrections at extreme angles as well as at nadir over four different MISR orbits (O012937, O013010, O013039 and O013068): data from Da, Df, and An cameras were used. Fig. 1 shows six scatter-plots for the lowest correlative cases of

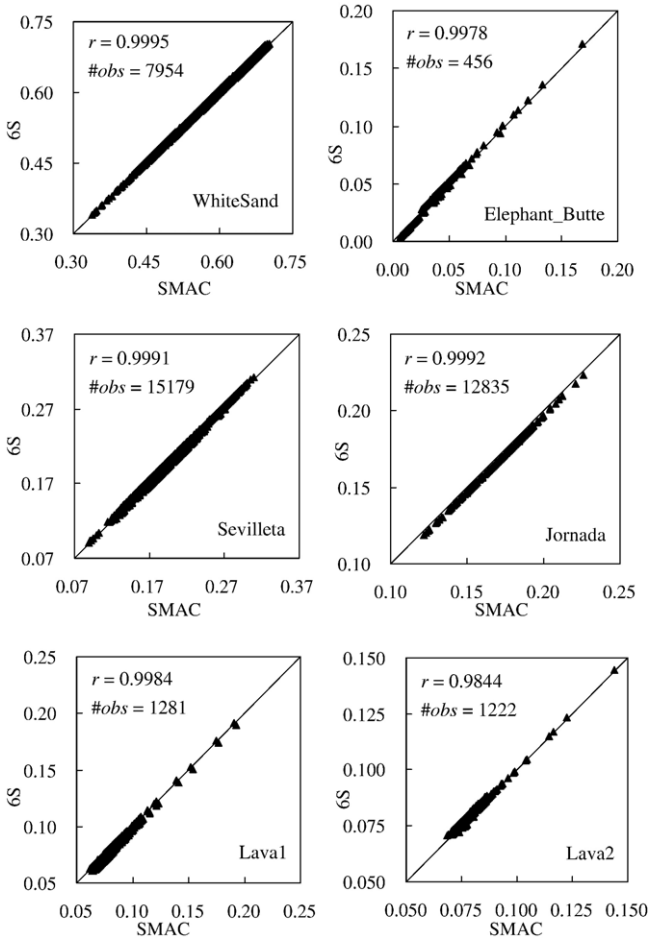

Fig. 1. The lowest correlation coefficients of 6S vs. SMAC on 6 testing areas at White Sands, Elephant Butte lake, Sevilleta, Jornada and two lava flows (r is a correlation coefficient, and #obs is number of observation).

the six testing areas. Regression analysis shows that the SMAC and 6S results are very similar: most correlation coefficients were greater than 0.992 with the lowest 0.984. More specifically, The Jornada, Sevilleta and White Sands always have correlation coefficients greater than 0.999. One of the lava flows provided the lowest correlation, but this lowest one is still high: 0.984. The other lava flow and Elephant Butte lake sites fall between these two extremes. While this does not resolve the question of the whether both modeling packages are in error at these geometries it does reduce one source of uncertainty: using SMAC instead of a more complete realization of an atmospheric modeling code.

3.3. Support vector machine

The foundations of the SVM approach were developed by Vapnik (1995) and are gaining popularity due to many attractive features and excellent empirical performance. The SVM training algorithm promises to obtain the optimal separating hyper-plane for a training data set in term of generalization error. Given a set of examples (x_i,y_i), $i=1,...l$ where $x_i \in R^N$ and $y_i \in \{-1,+1\}$. The support vector machines require the solution of the following optimization problem (Eq. (3)):

$$\min_{w,b,\xi}\left(\frac{1}{2}w^T\cdot w + C\sum_{i=1}^{l}\ \xi_i\right) \tag{3}$$

subject to $y_i(w^T\cdot\phi(x_i)+b)\geq 1-\xi_i$, $\xi_i\geq 0$. Here ξ_i are positive slack variables. $C>0$ is a preset penalty value for misclassification errors. Training vector x_i is mapped into a higher (maybe infinite) dimensional space by the function ϕ. The $w^T\cdot\phi(x_i)+b$ is a hyper-plane in this higher dimensional space. SVM will find an optimal separating hyper-plane. Furthermore, $k(x_i,x_j)=\phi(x_i)^T\phi(x_j)$ is called the kernel function. The choice of the kernel function k is crucial for good classification performance. In the study we used the radial basis function (RBF) (Eq. (4)):

$$k(x_i,x_j) = \exp(-\gamma\cdot||x_i-x_j||^2), \gamma>0 \tag{4}$$

Here, γ is a kernel parameter. The RBF is one of the most commonly used kernel functions. In general, the RBF is a reasonable choice. First, the RBF kernel non-linearly maps samples into a higher dimensional space, so the RBF can handle the case when the relationship between class labels and attributes is non-linear. Second, the RBF kernel has less numerical computation difficulties. We use LIBSVM software (Chang & Lin, 2001) in the experiments.

The following three procedures were used in the experiments: first, we conduct a simple scaling on the data; second, we manually search the best parameter C and γ on the training set; and finally, we use the best parameter C and γ to test accuracy and calculate the kappa index on the test set. There are two main advantages in scaling before applying the SVM algorithm: one is to avoid the case where attributes in greater numeric ranges dominate those in smaller numeric ranges. Another is to avoid

numerical difficulties during the calculation. Linear scaling each attribute to the range [−1,+1] or [0, 1] is recommended (Chang & Lin, 2001).

4. Results and discussion

The experiment area covered by the Jornada and Sevilleta vegetation maps produced by the respective LTERs is 23,978 pixels (250 m spatial resolution) in total, around 1492.4 km^2. Half of the area (11,984 pixels) was randomly picked up as a training set and the other half (11,994 pixels) was retained as the testing set for MLC and SVM classifications. There are 19 classes for these classification experiments, where 6 classes are from the Jornada and 13 classes from the Sevilleta (Table 1). Although the Jornada vegetation map has 9 classes, the numbers of pixels for the "Bare", "Snakeweed" and "Yucca" classes were too low for the classification experiments. The Jornada Experimental Range vegetation map uses a set of class names that differ from those used for the Sevilleta National Wildlife Refuge vegetation map. This might lead to a misunderstanding that the two study areas have completely different vegetation classes; however, both sites are within the Chihuahuan Desert and a number of the shrub and grass communities are similar (e.g., grama grass; creosotebush), or could feasibly exist at both locations. We therefore retained all classes. It is reasonable to classify the two study areas together because we expect the classifiers to exploit the canopy structure information carried by the MISR data: at a minimum this will show whether this additional information leads to lower classification confusion between grass and shrub communities over large areas.

In all some 44 classification experiments were performed and the results are listed in Tables 2–7. Tables 2 and 3 show the best candidate data sets for running MLC and SVM, while Tables 4–7 show the results of MLC and SVM classifications on these data sets and their combinations. It is well known that MLC does not work well if the probability distribution requirement is not satisfied. SVM, however, does not require any probability distributions. It is obvious that the requirement of MLC is much stricter than that of SVM, so we used only MLC to obtain the optimal combinations in Tables 2 and 3. We compared SVM with MLC based on same inputs in Tables 4–7.

Table 1
The 6 classes of the Jornada and 13 classes of the Sevilleta

Code	Class
1	jer_Upland_Grasses
2	jer_Playa_Grasses
3	jer_Tarbush
4	jer_Mesquite
5	jer_Creosotebush
6	jer_Other_Shrubs
7	sev_Water_or_Wet_Ground
8	sev_Barren_or_Sparsely_Vegetated
9	sev_Great_Basin_Grasslands
10	sev_Transition_Chihuahuan_and_Great_Basin_Grasslands
11	sev_Chihuahuan_Desert_Grasslands
12	sev_Transition_Chihuahuan_and_Plains_Grasslands
13	sev_Plains_Grasslands
14	sev_Chihuahuan_or_Great_Basin_LowlandSwale_Grasslands
15	sev_Chihuahuan_Desert_Shrublands
16	sev_Great_Basin_Shrublands
17	sev_Rocky_Mountain_Conifer_Savanna
18	sev_Rocky_Mountain_Conifer_Woodlands
19	sev_Rio_Grande_Riparian_Woodlands

Table 2
Maximum likelihood classifications at MISR data for selecting data sets

Pure MISR data set	Average TD	Overall accuracy	Kappa index
Nadir blue, green, red, NIR	1634.14	45.81	41.13
9 camera red	1778.13	41.93	36.26
Nadir 4 bands, and 8 off-nadir camera red	1912.70	56.78	52.19
9 camera red and NIR	1956.63	54.78	49.81
Nadir 4 bands, and D camera red/NIR	1858.64	48.54	43.79
Nadir 4 bands, and C camera red/NIR	1842.70	55.56	51.11
Nadir 4 bands, and B camera red/NIR	1820.81	56.49	52.14
Nadir 4 bands, and A camera red/NIR	1788.25	54.33	49.96
Nadir 4 bands, and C/B camera red/NIR	1907.82	58.34	53.81
Nadir 4 bands, and C/B/A camera red/NIR	1938.09	60.91	56.52
Nadir 4 bands, and D/C/B camera red/NIR	1956.66	55.52	50.72
Nadir 4 bands, and 8 off-nadir camera red/NIR	1969.48	59.38	54.78

The experiments with various combinations of MISR nadir and off-nadir reflectance are listed in Table 2. MISR nadir reflectance in the 4 spectral bands does not provide high accuracy. All 9 cameras in the red and near infrared bands can improve accuracy but as before do not achieve the highest accuracy. After trying various combinations of nadir and multi-angular reflectance, we found that the combination of the 4 multi-spectral (blue, green, red and near infrared) nadir reflectance and off-nadir (Cf, Bf, Af, Aa, Ba, Ca camera) reflectance in the red and near infrared bands can obtain the highest accuracy. Therefore we used this combination as the fundamental MISR multi-angular dataset. This dataset is called "MISR multi-angular plus". The MISR nadir reflectance in all 4 spectral bands is called "MISR nadir plus" for the subsequent experiments.

The experimental results in Table 3 show the capability of surface anisotropy patterns derived from the MRPV and RTnLS models. These BRDF parameters were obtained via inverting the two models against all MISR 9 multi-angle reflectance in the

Table 3
Maximum likelihood classifications at surface anisotropy patterns from MRPV model and RTnLS model

BRDF Model Data set	Average TD	Overall accuracy	Kappa index
MRPV *ρ0kb* red	1264.31	34.51	29.20
MRPV *ρ0kb* NIR	965.57	22.22	16.88
MRPV *ρ0kb* red/NIR	1578.71	42.95	37.82
RTnLS *isovolgeo* red	1322.08	37.35	32.09
RTnLS *isovolgeo* NIR	1227.85	27.02	22.24
RTnLS *isovolgeo* red/NIR	1625.01	43.45	38.84

Table 4
Maximum likelihood classifications at combinations of MISR data and the *k* parameter at red band of MRPV model and the Structural Scattering Index

Data set		Average TD	Overall accuracy	Kappa index
MISR nadir plus	None	1634.14	45.81	41.13
	*k*_red	1698.42	51.62	47.07
	SSI	1691.01	46.65	41.93
	*k*_red and SSI	1745.41	51.56	47.02
MISR multi-angle plus	None	1956.66	60.91	56.52
	*k*_red	1943.00	61.96	57.61
	SSI	1944.06	61.10	56.71
	*k*_red and SSI	1948.90	61.77	57.42

Table 6
Support vector machine classifications at combinations of MISR data and the k parameter at red band of MRPV model and the Structural Scattering Index

Data set		Overall accuracy	Kappa index
MISR nadir plus	None	64.31	59.09
	*k*_red	67.12	62.41
	SSI	66.15	61.22
	*k*_red and SSI	68.70	63.80
MISR multi-angle plus	None	75.56	72.21
	*k*_red	75.62	72.24
	SSI	75.83	72.50
	*k*_red and SSI	75.71	72.21

red and NIR bands. The lower spatial resolution of the NIR band may be a potential reason for the lower classification accuracies seen when using this band with the retrieved BRDF patterns vs. using only the red band. The combinations of surface anisotropy patterns in the red and near infrared bands provide higher capability than any single one of them, though the accuracy still is low. We also found two optimal data sets for the subsequent experiments: (1) surface anisotropy patterns at both the red and NIR bands derived from MRPV model, *ρ0kb*_red/NIR; (2) surface anisotropy patterns at the red and NIR bands derived from RTnLS model, *isovolgeo*_red/NIR (Table 3).

MLC methods were used to generate the results in Tables 4 and 5. Due to the probability distribution requirement of MLC, these results are suitable for estimating improvements from various inputs. Table 4 demonstrates the suitability of the *k* parameter of the MRPV model at the red band and the SSI from the RTnLS model as additional information dimensions in classification. The *k* parameter can raise by almost 6% the accuracy when it is used with the MISR nadir plus. The improvement is much bigger than when using the SSI. The improvement from the MISR nadir plus to the combinations of the MISR nadir plus and the *k* parameter or the SSI is greater than cases of the MISR multi-angle plus. It shows some information redundancy between MISR multi-angle reflectance and the additional information from the *k* parameter or the SSI. Using the *k* parameter or the SSI together cannot provide extra improvement. It means that two parameters are not compatible. Table 5 shows that — in comparison with Table 4 — these two parameters are not as good as the surface anisotropy patterns described by the *ρ0*, *k*, *b* of the MRPV model or the iso, vol, geo of the RTnLS model. The RTnLS model enjoys a slightly higher improvement than the MRPV model for this application. The combination of MISR nadir plus and the *isovolgeo*_red/NIR provides even higher accuracy than the original MISR multi-angular reflectance. It is 61.97% vs. 60.91%. Moreover, the *ρ0kb*_red/NIR and the *isovolgeo*_red/NIR each contain slightly different, unique information. In other words, using the *ρ0kb*_red/NIR and the *isovolgeo*_red/NIR together can obtain extra enhancement. The accuracy is 64.85% for case of the MISR nadir plus and the *ρ0kb*_red/NIR and the *isovolgeo*_red/NIR together. It is an increment of about 19% from the MISR nadir plus (64.85% vs. 45.81%). It is obvious that these BRDF parameters from the MRPV and the RTnLS models do carry useful information for classification. For cases of the MISR multi-angle plus, the *ρ0kb*_red/NIR and the *isovolgeo*_red/NIR together raise accuracy only 7.2% from 60.9% to 68.1%. It means that there is greater information redundancy between MISR multi-angle reflectance and the additional information from the *ρ0kb*_red/NIR and the *isovolgeo*_red/NIR. In summary, Tables 4 and 5 show: 1) original multi-angular reflectance can raise classification accuracy from 45.8% for nadir-only reflectance to 60.9%; 2) with surface anisotropy patterns derived from MRPV and RTnLS, an accuracy of 68.1% can be obtained. Totally, an increment of 22.3% has been obtained with multi-angle reflectance and the derived BRDF parameters.

Tables 6 and 7 display results from SVM methods. They use the same input as Tables 4 and 5, respectively; the only difference between the two table groups is the classification algorithm. In comparison with Tables 4–7 are suitable for estimating improvements from SVM. The two table groups

Table 5
Maximum likelihood classifications at combinations of MISR data and surface anisotropy pattern inversed by BRDF models from MISR data

Data set		Average TD	Overall accuracy	Kappa index
MISR nadir plus	*ρ0kb*_red/NIR	1862.14	56.61	52.33
	*isovolgeo*_red/NIR	1881.44	61.97	58.00
	*ρ0kb_isovolgeo*_red/NIR	1954.38	64.85	60.96
MISR multi-angle plus	*ρ0kb*_red/NIR	1970.38	64.45	60.31
	*isovolgeo*_red/NIR	1972.70	65.54	61.51
	*ρ0kb_isovolgeo*_red/NIR	1987.85	68.14	64.31

Table 7
Support vector machine classifications at combinations of MISR data and surface anisotropy pattern inversed by BRDF models from MISR data

Data set		Overall accuracy	Kappa index
MISR nadir plus	*ρ0kb*_red/NIR	72.10	68.16
	*isovolgeo*_red/NIR	74.62	71.06
	*ρ0kb_isovolgeo*_red/NIR	75.62	72.22
MISR multi-angle plus	*ρ0kb*_red/NIR	75.67	72.31
	*isovolgeo*_red/NIR	76.60	73.38
	*ρ0kb_isovolgeo*_red/NIR	76.73	73.50

show roughly similar trends in accuracy improvement when various inputs were brought into play. The *k* parameter of the MRPV model and the SSI from the RTnLS model provide additional information to classification, but the improvement is marginal. However, the *ρ0*, *k* and *b* of the MRPV model or the iso, vol and geo of the RTnLS model carry useful information. Using the *ρ0kb*_red/NIR and the *isovolgeo*_red/NIR with the MISR nadir plus together, we can obtain 75.62% accuracy. It is very close to the highest accuracy (76.73%), which was found with the combination of the MISR multi-angle plus, the *ρ0kb*_red/NIR and the *isovolgeo*_red/NIR. As mentioned above, the MLC also obtained its highest accuracy under the same conditions. For cases of the *k* parameter or/and the SSI, the SVM always raised accuracy more than 15% for cases of the MISR nadir plus, and between 13% and 15% for the MISR multi-angle plus. On the *ρ0kb*_red/NIR or/and the *isovolgeo*_red/NIR, the improvements are roughly from 8% to 15%. The mean of all of improvements is round 14%. These results show that the SVM algorithm exploits the information carried by the same inputs more effectively. The smallest increment (8%) occurs in the case of the highest classification accuracy (from 76.73% to 68.1%). At this point, we can speculate that the probability distributions of classes were enhanced to a great degree when combining the *ρ0kb*_red/NIR, the *isovolgeo*_red/NIR, and the MISR off-nadir reflectance with the MISR nadir reflectance. Thus the MLC method using multi-angle data obtains a large improvement over spectral data alone (19% increment from 45.81% to 64.85%), leaving less potential for SVM methods.

It is informative to compare the relative performance of the same method with different inputs, and of different methods with same inputs on a class-by-class basis. The contingency matrices obtained by the MLC with the MISR nadir plus, and with the combination of the MISR multi-angle plus, the *ρ0kb*_red/NIR and the *isovolgeo*_red/NIR are shown in Tables 8 and 9, respectively. With same inputs as Table 9, contingency matrices obtained by the SVM are shown in Table 10. While overall accuracy is the number of pixels correctly classified divided by the total number of pixels in the training data set, the user's accuracy is a measure of how well the classification performed by class and details errors of commission (pixels assigned to incorrect classes). Of the MLC results, the class-level user's accuracies obtained with multi-angle data (Table 9) are almost all much better than the corresponding ones obtained with nadir data (Table 8). Among the 19 classes, 'JER upland grasses', 'JER Other shrubs', 'SEV Water/wet ground', and 'SEV Great Basin shrublands' (classes 1, 6, 7 and 16, respectively) all enjoy a huge improvement as a result of incorporating the multi-angle reflectance and the surface anisotropy patterns. The only reduction in user's accuracy was for class 4 ('JER mesquite'): its accuracy was reduced from 94.1% to 90.5% — this is still very acceptable.

The questions of why and how nadir data with the MLC method produces such grave misclassifications can be addressed by examining the classes with which confusion occurred. Classes 1, 2, and 6 were all subject to misclassification as class 4 ('JER Mesquite'). This is quite astonishing — many pixels for two grassland communities were assigned to a shrub-dominated community class — and highlights the limitations of nadir-spectral data in this environment. The misclassification of upland and playa grasses as shrubland is surprising because the fractions of exposed soil and canopy physical structure which largely determine the spectral signal are very different between grasslands and shrublands. It is less surprising that class 6 ('JER Other shrubs') would be misclassified as 'JER mesquite' shrubland. The dramatic improvements in differentiating these classes when using MISR multi-angle data are perhaps not surprising since the

Table 8
Contingency matrix of the maximum likelihood classification on MISR nadir plus

Classes	1	2	3	4	5	6	7	8	9	10	11	12	13	14	15	16	17	18	19	Sum	User's
1	**54**	18	53	94	75	0	0	0	0	11	1	7	0	2	1	0	0	0	0	316	**17.1**
2	3	**67**	12	221	90	0	0	1	2	1	2	0	0	1	4	0	1	0	0	405	**16.5**
3	3	21	**190**	124	161	0	0	0	6	5	2	12	0	2	7	1	0	0	0	534	**35.6**
4	1	1	3	**1383**	71	4	0	0	0	0	0	0	0	0	0	0	0	0	0	1470	**94.1**
5	2	12	17	79	**400**	6	0	0	21	3	20	4	0	2	39	14	5	0	0	624	**64.1**
6	7	4	2	968	188	**39**	0	0	0	0	2	0	0	0	5	0	0	0	0	1215	**3.2**
7	0	3	0	10	3	0	**27**	22	25	5	17	4	0	0	26	34	24	1	2	203	**13.3**
8	0	0	0	0	0	0	5	**217**	165	23	82	3	0	0	33	32	2	0	0	562	**38.6**
9	0	1	0	0	5	0	1	103	**986**	77	116	27	0	16	169	154	16	0	2	1673	**58.9**
10	0	2	2	1	35	0	0	8	106	**514**	35	104	3	21	113	35	4	0	0	983	**52.3**
11	0	0	1	1	8	0	0	7	27	11	**73**	12	4	5	25	3	21	0	0	198	**36.9**
12	0	2	3	0	21	0	0	6	43	160	36	**282**	28	6	12	16	22	0	1	638	**44.2**
13	0	0	0	0	1	0	0	1	1	71	45	138	**163**	2	25	4	87	0	1	539	**30.2**
14	1	5	7	12	19	0	0	9	49	56	77	25	6	**54**	105	1	9	0	0	435	**12.4**
15	0	2	3	4	31	0	2	6	26	58	35	20	1	6	**98**	27	3	0	3	325	**30.2**
16	0	2	0	2	29	0	12	27	195	63	79	27	1	3	121	**164**	47	0	7	779	**21.1**
17	0	1	1	6	32	0	2	1	6	1	27	20	22	3	8	9	**510**	10	6	665	**76.7**
18	0	0	0	0	0	0	0	0	1	0	0	0	0	0	0	1	103	**228**	5	338	**67.5**
19	0	0	0	0	0	0	4	2	2	0	5	1	0	1	0	4	19	9	**45**	92	**48.9**
Sum	71	148	294	2905	1169	49	53	410	1661	1059	654	686	228	124	791	499	873	248	72	11994	
Producer's	**76.1**	**45.3**	**64.6**	**47.6**	**34.2**	**79.6**	**50.9**	**52.9**	**59.4**	**48.5**	**11.2**	**41.1**	**71.5**	**43.6**	**12.4**	**32.9**	**58.4**	**91.9**	**62.5**		**45.8**

Table 9
Contingency matrix of the maximum likelihood classification on combinations of MISR multi-angle plus and surface anisotropy patterns at red and near infrared bands

Classes	1	2	3	4	5	6	7	8	9	10	11	12	13	14	15	16	17	18	19	Sum	User's
1	**53**	7	0	24	0	0	0	0	0	0	0	0	0	0	0	0	0	0	0	84	**63.1**
2	6	**94**	6	192	6	0	0	0	0	0	0	0	0	0	0	0	0	0	0	304	**30.9**
3	3	19	**271**	116	124	0	0	0	1	0	0	0	0	0	0	0	0	0	0	534	**50.7**
4	7	21	5	**2430**	203	18	0	0	0	0	0	0	0	0	0	0	0	0	0	2684	**90.5**
5	1	7	11	114	**829**	8	0	0	0	0	0	0	0	0	0	0	3	0	0	973	**85.2**
6	0	0	0	18	4	**23**	0	0	0	0	0	0	0	0	0	0	0	0	0	45	**51.1**
7	0	0	0	0	0	0	**34**	1	4	0	0	0	0	1	0	13	5	0	6	64	**53.1**
8	0	0	0	0	0	0	7	**237**	87	10	21	2	0	2	24	24	12	0	0	426	**55.6**
9	0	0	0	0	0	0	0	64	**1130**	39	24	21	1	13	165	74	21	0	2	1554	**72.7**
10	0	0	0	0	0	0	0	7	34	**797**	49	94	8	10	112	2	1	0	0	1114	**71.5**
11	0	0	0	0	0	0	0	43	59	59	**416**	57	10	10	197	6	175	0	2	1034	**40.2**
12	0	0	0	0	0	0	0	1	11	82	24	**401**	42	3	3	4	19	0	0	590	**68.0**
13	0	0	0	0	0	0	0	0	1	3	12	61	**149**	1	5	0	110	0	0	342	**43.6**
14	0	0	0	0	0	0	0	6	82	39	42	15	7	**76**	61	6	3	0	0	337	**22.6**
15	0	0	0	0	0	0	2	22	59	27	52	19	0	6	**203**	10	18	0	1	419	**48.4**
16	1	0	1	1	2	0	6	26	176	3	4	4	1	1	15	**345**	20	0	3	609	**56.7**
17	0	0	0	10	1	0	0	1	8	0	6	7	9	0	5	3	**428**	44	5	527	**81.2**
18	0	0	0	0	0	0	0	0	0	0	0	0	1	0	0	0	56	**204**	0	261	**78.2**
19	0	0	0	0	0	0	4	2	9	0	4	5	0	1	1	12	2	0	**53**	93	**57.0**
Sum	71	148	294	2905	1169	49	53	410	1661	1059	654	686	228	124	791	499	873	248	72	11994	
Producer's	**74.6**	**63.5**	**92.2**	**83.6**	**70.9**	**46.9**	**64.2**	**57.8**	**68.0**	**75.3**	**63.6**	**58.5**	**65.4**	**61.3**	**25.7**	**69.1**	**49.0**	**82.3**	**73.6**		**68.1**

multi-angle data and metrics hold greater information on canopy structure. This information is derived mainly from the change in the proportion of shadowed soil in the MISR field-of-view in different cameras.

The SVM further improved the classification using the same MISR multi-angle data (the MISR multi-angle plus, the *ρ0kb*_red/NIR and the *isovolgeo*_red/NIR). The class-level user's accuracies obtained with the multi-angle/SVM (Table 10) are almost all much better than the corresponding ones obtained with the multi-angle/MLC (Table 9). Among the 19 classes, 'JER Playa grasses', 'JER Tarbush' and 'SEV Plains grassland' (classes 2, 3 and 13, respectively) enjoy a huge improvement as a result of using the SVM. The only reduction in user's accuracy was for class 9 ('SEV Great Basin shrublands'): its accuracy was reduced from 72.7% to 69.2%; as before, this is not unacceptably low.

The worst case obtained with the multi-angle/SVM method occurred with respect to class 14 ('SEV Chihuahuan or Great Basin lowland swale grasslands'); the user's accuracy was still low even though it was raised some 16.7 percentage points from 22.6% to 39.3%. This class was inclined to be confused with classes 9, 10, 11, 12 and 15 in the both the multi-angle/MLC

Table 10
Contingency matrix of the support vector machine classification on combinations of MISR multi-angle plus and surface anisotropy patterns at red and near infrared bands

Classes	1	2	3	4	5	6	7	8	9	10	11	12	13	14	15	16	17	18	19	Sum	User's
1	**47**	1	2	7	1	0	0	0	0	0	0	0	0	0	0	0	0	0	0	58	**81.0**
2	1	**57**	1	11	1	0	0	0	0	0	0	0	0	0	0	0	0	0	0	71	**80.3**
3	3	10	**231**	39	47	0	0	0	0	0	0	0	0	0	0	0	0	0	0	330	**70.0**
4	19	67	33	**2795**	130	27	0	0	0	0	0	0	0	0	0	1	0	0	0	3072	**91.0**
5	1	13	25	50	**985**	10	0	0	0	0	0	0	0	0	0	0	0	0	0	1084	**90.9**
6	0	0	0	2	4	**12**	0	0	0	0	0	0	0	0	0	0	0	0	0	18	**66.7**
7	0	0	0	0	0	0	**26**	2	1	0	0	0	0	0	0	4	4	0	5	42	**61.9**
8	0	0	1	0	0	0	6	**223**	42	3	16	2	0	0	15	7	3	0	0	318	**70.1**
9	0	0	0	0	0	0	3	101	**1415**	49	52	31	1	31	199	145	17	0	0	2044	**69.2**
10	0	0	0	0	0	0	1	13	17	**846**	36	77	2	15	95	5	3	0	1	1111	**76.2**
11	0	0	0	0	0	0	0	20	25	36	**356**	15	4	11	135	5	34	0	4	645	**55.2**
12	0	0	0	0	0	0	0	1	9	78	24	**467**	41	5	2	4	15	0	1	647	**72.2**
13	0	0	0	0	0	0	0	0	0	0	1	41	**136**	1	0	0	25	0	0	204	**66.7**
14	0	0	0	0	0	0	0	1	14	7	15	14	2	**44**	9	3	1	0	2	112	**39.3**
15	0	0	0	0	0	0	2	31	59	35	111	13	4	14	**323**	14	12	0	1	619	**52.2**
16	0	0	0	0	1	0	9	12	70	2	1	1	0	1	4	**295**	8	0	8	412	**71.6**
17	0	0	1	1	0	0	2	5	8	3	39	22	38	2	9	10	**705**	43	3	891	**79.1**
18	0	0	0	0	0	0	0	0	0	0	0	0	0	0	0	0	46	**205**	0	251	**81.7**
19	0	0	0	0	0	0	4	1	1	0	3	3	0	0	0	6	0	0	**47**	65	**72.3**
Sum	71	148	294	2905	1169	49	53	410	1661	1059	654	686	228	124	791	499	873	248	72	11994	
Producer's	**66.2**	**38.5**	**78.6**	**96.2**	**84.3**	**24.5**	**49.1**	**54.4**	**85.2**	**79.9**	**54.4**	**68.1**	**59.7**	**35.5**	**40.8**	**59.1**	**80.8**	**82.7**	**65.3**		**76.7**

classification and the multi-angle/SVM classification: this is not so surprising as all these except the last are grassland classes; and the total number of pixels is small (112), reducing the statistical significance of the result. With the multi-angle/SVM classification the incorrectly classified pixels of classes 9, 10, 11, 12, 14 and 15 almost all fall amongst these same classes, implying that there is more difficulty in differentiating amongst the grasslands of the Sevilleta National Wildlife Refuge (Table 10). In general, the grass, shrub and woodland community types of the Sevilleta were not confused; similarly, the JER vegetation community types were rarely confused with the SEV vegetation community types. It is worth noting that the worst case per-class user's accuracies obtained when nadir-spectral data were used were much lower: 3.2%, 12.4%, 13.3%, 16.5%, and 17.1% (for classes 6, 14, 7, 2, and 1, respectively).

This is a robust demonstration of the tangible improvements obtained with multi-angle reflectance, the derived BRDF parameters, and SVM algorithms when a wide range of cover types is included. These data can be treated in the same way. In MLC, different input parameters will be projected to different axis in a multi-dimensional classification space. In SVM, all input parameters will be scaled to [−1,1]. Therefore, different units of input parameters will not affect classification. On the basis of these results much greater confidence would be expected in classification of multi-angle remote sensing data to recognized community and cover types over larger areas outside the environs of the study areas, especially if SVM methods are used. These experiments show that the surface anisotropy patterns described by the MRPV and RTnLS models are compatible with each other; when they are used together better

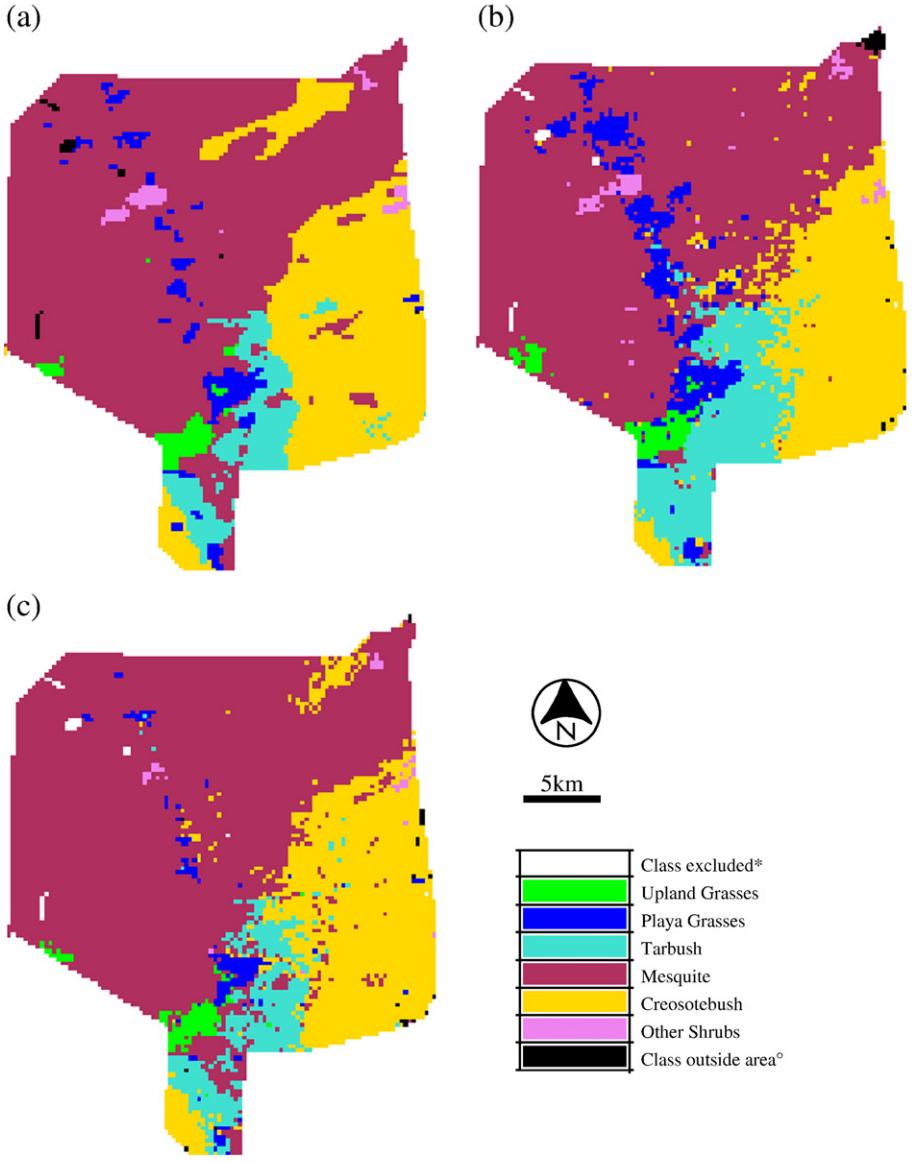

Fig. 2. Community Type Classifications for the Jornada Experimental Range (a) 1998 LTER Vegetation Map (b) Maximum Likelihood method (c) Support Vector Machine Method. Note: * Areas corresponding to classes for which there were insufficient data to perform a classification. ° Classification as a class belonging to the Sevilleta.

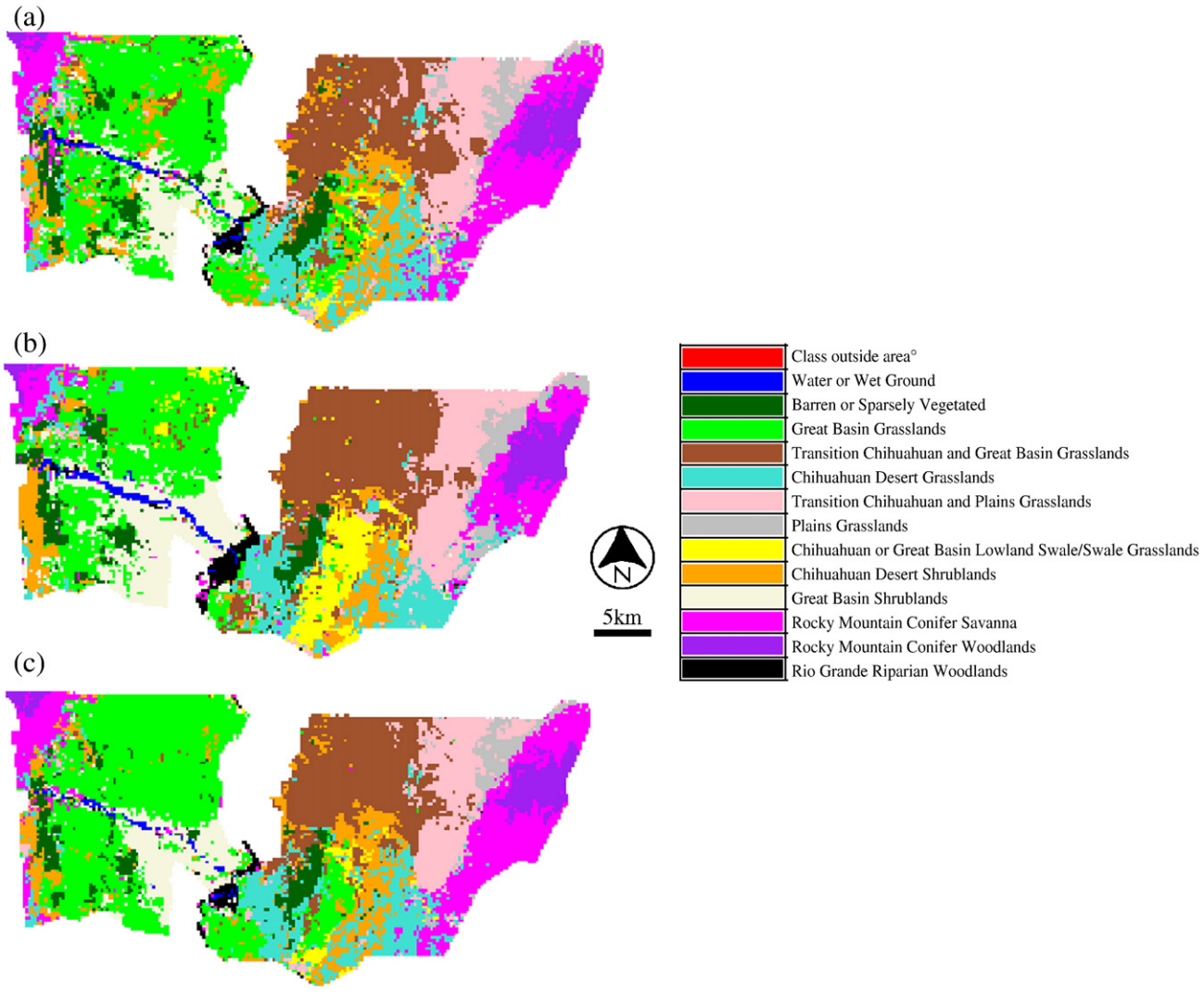

Fig. 3. Community Type Classifications for the Sevilleta National Wildlife Refuge (a) 1998 LTER Vegetation Map (b) Maximum Likelihood method (c) Support Vector Machine Method. Note: ° Classified as a class belonging to the Jornada.

results can always be obtained. The combinations of MISR nadir reflectance and surface anisotropy patterns from inversion of BDRF models can provide the same accuracy as the original MISR multi-angular reflectance. In fact, this suggests an innovative approach to improve classification and fusion data from multiple satellites. For example, multi-angle reflectance from MISR, MODIS, and SPOT VEGETATION (amongst others) could be used to obtain more precise surface anisotropy patterns though the RTnLS and MRPV model inversions; these might then be combined with nadir reflectance from MISR and even higher resolution instruments such as ASTER for classification. Better results might be expected with this kind of approach.

Figs. 2 and 3 show the vegetation maps and the MLC and SVM classification maps with the best overall accuracies for the Jornada Experimental Range and the Sevilleta National Wildlife Refuge, respectively. As mentioned before, the highest MLC accuracy is 68.1%, and the highest SVM accuracy is 76.7%. The two methods use same inputs. Note that these accuracies are overall accuracies; Kappa index values show a similar trend to overall accuracies indicating that the results are not spurious. In addition, no auxiliary information on (for example) soils and terrain slope and aspect has been used in these experiments.

5. Conclusions

The conclusions of this research can be summarized as follows:

(1) In the classification experiments, additional information is provided by the $\rho 0$, k, and b parameters from the MRPV model and the iso, vol and geo parameters from the RTnLS model in the red and NIR bands. In other words, the whole shape of the BRDF provides more information than any one of the parameters, which describe the shape in either of these two models.
(2) The highest classification accuracy is expected to be obtained by using the following data together: 1) MISR nadir blue and green red and NIR reflectance; 2) multi-angular (C, B, A camera) red and NIR reflectance; 3) the

$\rho 0$, k, b parameters of the MRPV model, and the iso, vol, geo parameters of the RTnLS model at red and NIR bands.

(3) The combination of MISR nadir reflectance and surface anisotropy patterns obtained by inversion of BDRF models can provide almost the same accuracy as obtained with the original MISR multi-angle reflectance.
(4) The k parameter of the MRPV model and the SSI from the RTnLS model provide additional information to the classification problem — but the improvement is marginal.
(5) Multi-angle reflectance provides more information on the surface than nadir-spectral reflectance alone.
(6) Reflectance in the NIR are helpful in differentiating semi-desert vegetation types even though these data are obtained at 1.1 km spatial resolution and the contrast between soil and vegetation components is lower than in the red wavelengths (arid regions have bright mineral soils).
(7) Using SVM algorithms provide a marked improvement over the parametric MLC methods for classification of semi-arid vegetation types.

While the best overall classification accuracy obtained might not be considered high in the context of mapping broad land cover classes, we are here concerned with plant communities that exhibit a wide range of within-community conditions. Future work will therefore explore the use of a soft classification approach based on fuzzy set theory as well as the integration of relatively static auxiliary data on soils and topography. Recent work on retrieving fractional woody shrub cover via geometric-optical modeling (Chopping et al., in press) will also provide information that will mitigate against confusion owing to within-community variation; for example, enabling differentiation of grama grass communities that exhibit differing degrees of woody shrub encroachment.

Acknowledgments

This research was supported by the National Aeronautics and Space Administration (EOS grant # NNG04GK91G to Chopping, administered through the NASA Land Cover Land Use Change program, Program Manager: Garik Gutman). The Jornada and Sevilleta vegetation map were provided by the Jornada Basin and the Sevilleta Long-Term Ecological Research (LTER), respectively; funding for these data was provided by the US National Science Foundation.

Appendix A

The procedures employed for the processing of the three MISR data products were as follows:

(1) The solar constant and SOM projection parameters were extracted for any given orbit.
(2) The blocks that overlap the working region were calculated, given geographic coordinates of 4 corners of our working region.
(3) Top of atmosphere (TOA) radiance data for these blocks obtained at step (2) were extracted from the MI1B2T products. The radiance data include: 1) 275 m four bands nadir radiance; 2) 275 m red band off-nadir radiance and 3) 1.1 km near infrared band off-nadir radiance. The radiance data are indexed by MISR (block, block-relative line, block-relative sample) coordinates.
(4) Aerosol data for the blocks obtained at step (2) were extracted from the MIL2ASAE products. These data have 17.6 km spatial resolution and are also indexed by MISR (block, block-relative line, block-relative sample) coordinates.
(5) The solar zenith and azimuth and viewing zenith and azimuth for the blocks obtained at step (2) were extracted from the MI1B2GEOP products. They also have 17.6 km spatial resolution. These angle data are indexed by MISR (block, block-relative line, block-relative sample) coordinates.
(6) Atmospheric corrections were performed on the TOA radiance obtained at step (3) to obtain surface reflectance using the solar and viewing angles at step (4) and aerosol data at step (5). For each 17.6 km pixel, the atmospheric correction procedure was: a) sort the TOA radiances covered by the pixel; b) select 16 TOA radiances uniformly; c) run the SMAC for the 16 radiances to calculate their ground reflectance; d) regress these TOA radiance and their ground reflectance and e) apply the regression parameters to all other TOA radiances to obtain surface reflectance. Following TOA radiances, the surface reflectance also are indexed by MISR (block, block-relative line, block-relative sample) coordinates.
(7) The surface reflectance, solar angles, observing angles and aerosol data were resampled to a 250 m grid in the UTM projection. There were two steps: first, the data were transformed from MISR stacked-grid index (block, block-relative line, block-relative sample) to geographic coordinates (latitude, longitude) through the 3-phase method described before; and second, the data were projected from geographic coordinates (latitude, longitude) to UTM coordinates (X, Y) and resampled to 250 m using a nearest neighbor algorithm.
(8) Surface reflectance, solar zenith and azimuth angles, and viewing zenith and azimuth angles of the 9 cameras were collected for red and near infrared bands for all orbits to produce a MISR multi-angle reflectance dataset.
(9) BRDF parameters (iso, vol and geo) were produced via inverting the RossThin–LiSparseMODIS kernel-driven model against the MISR multi-angle reflectance dataset obtained at step (8).
(10) The structural scattering index was computed by using the parameters at step (9).
(11) BRDF parameters ($\rho 0$, k, b) were produced via inverting the Modified–Rahman–Pinty–Verstraete model against the dataset obtained at step (8).

References

Chang, C. C., & Lin, C. J. (2001). LIBSVM: A library for support vector machines. Software available at http://www.csie.ntu.edu.tw/~cjlin/libsvm

Chopping, M. J. (2001). Testing LiSK BRDF models over a semi-arid grassland region with visible and near-infrared ATSR-2 and AVHRR data. *International Journal of Remote Sensing*, *22*, 3533−3552.

Chopping, M. J., Rango, A., & Ritchie, J. C. (2002). Improved semi-arid community type differentiation with the NOAA AVHRR via exploitation of the directional signal. *IEEE Transactions on Geoscience and Remote Sensing*, *40*(5), 1132−1149.

Chopping, M., Su, L., Rango, A., Martonchik, J. V., Peters, D. P. C., & Laliberte, A. (in press). Remote sensing of woody shrub cover in desert grasslands using MISR with a geometric-optical canopy reflectance model. *Remote Sensing of Environment*.

Diner, D. J., Martonchik, J. V., Borel, C., Gerstl, S. A. W., Gordon, H. R., Knyazikhin, Y., et al. (1999). Multi-angle Imaging Spectro-Radiometer Level 2 Surface Retrieval Algorithm Theoretical Basis Document.http://eospso.gsfc.nasa.gov/eos_homepage/for_scientists/atbd/docs/MISR/atbd-misr-10.pdf December 2, 1999. Jet Propulsion Laboratory, California Institute of Technology.

Engelsen, O., Pinty, B., Verstraete, M. M., & Martonchik, J. V. (1996). *Parametric bidirectional reflectance factor models: Evaluation, improvements and applications.EC Joint Research Centre, Technical Report No. EUR 16426 EN*. 114 pp.

Gao, F., Schaaf, C. B., Strahler, A. H., Jin, Y., & Li, X. (2003). Detecting vegetation structure using a kernel-based BRDF model. *Remote Sensing of Environment*, *86*(2), 198−205.

Huang, C., Davis, L. S., & Townshend, J. R. G. (2002). An assessment of support vector machines for land cover classification. *International Journal of Remote Sensing*, *23*(4), 725−749.

Jensen, J. R. (1996). *Introductory digital image processing: A remote sensing perspective*, (2nd ed.). Upper Saddle River, New Jersey: Prentice Hall.

Keuchel, J., Naumann, S., Heiler, M., & Siegmund, A. (2003). Automatic land cover analysis for Tenerife by supervised classification using remotely sensed data. *Remote Sensing of Environment*, *86*(4), 530−541.

Lewicki, S., Moroney, C., Crean, K., Gluck, S., Miller, K., Smyth, M., et al. (2003). *MISR data products specifications December 12, 2003, NASA JPL/ California Institute of Technology.* 348 pp..

Morisette, J., Privette, J., Justice, C., Olsen, D., Dwyer, J., Davis, P., et al. (1999). The EOS land validation core sites: Background information and current status. *Earth Observer*, *11*, 26.

Muldavin, E., Shore, G., Taugher, K., & Milne, B. (1998). *A vegetation classification and map for the Sevilleta National Wildlife Refuge, New Mexico: Final report.* New Mexico Natural Heritage Program and Sevilleta Long Term Ecological Research Program, Biology Department, University of New Mexico, Albuquerque.

Nolen, B. A., Dinterman, P., Kenney, J. F., Jones, G., & Ayarbe, L. (1999). New digitize databases. *Proceedings of 9th Annual Jornada Symposium.* Las Cruces, NM, 1999.

Pal, M., & Mather, P. M. (2005). Support vector machines for classification in remote sensing. *International Journal of Remote Sensing*, *26*(5), 1007−1011.

Pinty, B., Wildlowski, J. L., Gobron, N., Verstraete, M. M., & Diner, D. J. (2002). Uniqueness of multiangular measurements — Part I: An indicator of subpixel surface heterogeneity from MISR. *IEEE Transactions on Geoscience and Remote Sensing*, *40*(7), 1560−1573.

Rahman, H., Pinty, B., & Verstraete, M. M. (1993). Coupled surface-atmosphere reflectance (CSAR) model. 2. Semi-empirical surface model usable with NOAA Advanced Very High Resolution Radiometer data. *Journal of Geophysical Research*, *98*, 20791−20801.

Rahman, H., Verstraete, M. M., & Pinty, B. (1993). Coupled surface-atmosphere reflectance (CSAR) model. 1. Model description and inversion on synthetic data. *Journal of Geophysical Research*, *98*, 20779−20789.

Rahman, H., & Dedieu, G. (1994). SMAC: A simplified method for the atmospheric correction of satellite measurements in the solar spectrum. *International Journal of Remote Sensing*, *15*(1), 123−143.

Rango, A., Richie, J. C., Kustas, W. P., Schmugge, T. J., & Havstad, K. M. (1998). JORNEX: Remote sensing to quantify long-term vegetation change and hydrological fluxes in an arid rangeland environment. In H. Wheater (Ed.), *Hydrology in a changing Environment* (pp. 585−590). New York: Wiley.

Ritchie, J. C., Schmugge, T. J., Rango, A. & Schiebe, F. R. (2000), Remote Sensing applications for monitoring semiarid grasslands at the Sevilleta LTER, New Mexico, in na, editor(s). *Proceedings of the IEEE 2000 International Geoscience and Remote Sensing Symposium*, 24–28 July 2000, Honolulu, Hawaii, Volume: V. Spring: IEEE GRSS, 1969–1971.

Roujean, J. L., Leroy, M., & Deschanps, P. Y. (1992). A bidirectional reflectance model of the Earth's surface for the correction of remote sensing data. *Journal of Geophysical Research*, *97*(D18), 20455−20468.

Schaaf, C. B., Gao, F., Strahler, A. H., Lucht, W., Li, X., Tsang, T., et al. (2002). First operational BRDF, albedo and nadir reflectance products from MODIS. *Remote Sensing of Environment*, *83*, 135−148.

Su, L., Li, X., Friedl, M., Strahler, A., & Gu, X. (2002). A kernel-driven model for effective directional emissivity for non-isothermal surfaces. *Progress in Natural Science*, *12*(8), 603−607.

Strahler, A. H., & Muller, J. P. (1999). MODIS BRDF/Albedo product: Algorithm theoretical basis document, version 5.0, April 1999. http://modis.gsfc.nasa.gov/data/atbd/atbd_mod09.pdf

Vapnik, V. (1995). *The nature of statistical learning theory.* New York, NY: Springer–Verlag.

Vermote, E., Tanre, D., Deuze, J. L., Herman, M., & Morcrette, J. J. (1997). Second simulation of the satellite signal in the solar spectrum, 6S: An overview. *IEEE Transactions on Geoscience and Remote Sensing*, *35*(3), 675−686.

Wanner, W., Li, X., & Strahler, A. H. (1995). On the derivation of kernels for kernel-driven models of bidirectional reflectance. *Journal of Geophysical Research*, *100*, 21077−21090.

Zhu, G., & Blumberg, D. G. (2002). Classification using ASTER data and SVM algorithms: The case study of Beer Sheva, Israel. *Remote Sensing of Environment*, *80*, 233−240.